



**HAL**  
open science

## Surface plasmonics of Weyl semimetals

Xin Lu, Dibya Kanti Mukherjee, Mark Goerbig

► **To cite this version:**

Xin Lu, Dibya Kanti Mukherjee, Mark Goerbig. Surface plasmonics of Weyl semimetals. *Physical Review B*, 2021, 104 (15), 10.1103/PhysRevB.104.155103 . hal-03372718

**HAL Id: hal-03372718**


**<https://hal.science/hal-03372718>**

Submitted on 13 Oct 2022

**HAL** is a multi-disciplinary open access archive for the deposit and dissemination of scientific research documents, whether they are published or not. The documents may come from teaching and research institutions in France or abroad, or from public or private research centers.

L'archive ouverte pluridisciplinaire **HAL**, est destinée au dépôt et à la diffusion de documents scientifiques de niveau recherche, publiés ou non, émanant des établissements d'enseignement et de recherche français ou étrangers, des laboratoires publics ou privés.

## Surface plasmonics of Weyl semimetals

Xin Lu <sup>1</sup>, Dibya Kanti Mukherjee,<sup>1,2</sup> and Mark O. Goerbig<sup>1</sup>

<sup>1</sup>Laboratoire de Physique des Solides, Univ. Paris-Sud, Université Paris Saclay, CNRS, UMR 8502, F-91405 Orsay Cedex, France

<sup>2</sup>Department of Physics, Indiana University, Bloomington, Indiana 47405, USA



(Received 5 May 2021; accepted 23 September 2021; published 4 October 2021)

Smooth interfaces of topological systems are known to host massive surface states in addition to the topologically protected chiral one. We show that in Weyl semimetals these massive states, along with the chiral Fermi arc, strongly alter the form of the Fermi-arc plasmon. Most saliently, they yield further collective plasmonic modes that are absent in a conventional interface. The plasmon modes are completely anisotropic as a consequence of the underlying anisotropy in the surface model and expected to have a clear-cut experimental signature, e.g., in electron-energy loss spectroscopy.

DOI: [10.1103/PhysRevB.104.155103](https://doi.org/10.1103/PhysRevB.104.155103)

### I. INTRODUCTION

Weyl semimetals (WSMs) are often considered as a three-dimensional (3D) version of graphene since their low-energy  $\mathbf{k} \cdot \mathbf{p}$  Hamiltonian is described by the massless Weyl equation with linear energy dispersion known as Weyl cones [1]. WSMs must have an even number of Weyl cones: at least four for inversion symmetry broken WSM and two for time-reversal symmetry broken ones. Previous studies have shown that the bulk dielectric properties such as Friedel oscillations and (magneto-)plasmons in WSMs [2–6] are different from those of graphene [7,8] due to the increased dimensionality. For example, the bulk plasmon's dispersion in WSMs is gapped and parabolic in momentum while it follows a gapless square-root dispersion in graphene. The chiral anomaly in WSMs [9] may be probed by the bulk plasmon [10] whose dispersion depends on the chirality-resolved chemical potential. As topological semimetals, WSMs can also host surface plasmons [11] and surface plasmon polaritons [12,13], as it was shown using Maxwell's equations in the bulk with a topological Chern-Simons  $\theta$ -term [14]. In particular, in ferromagnetic WSMs, due to its gapless spectrum and large Berry curvature [15,16], electromagnetic waves propagate nonreciprocally, i.e., one direction is preferred.

Localized surface states can also give birth to original surface plasmons. In WSMs, topologically protected Fermi-arc (FA) states connecting two Weyl cones emerge at the surface due to the bulk-edge correspondence: The presence of topologically protected edge states is dictated by the topological invariant of the twisted bulk band structure. The FA states have been shown to induce a chiral linear FA surface plasmon with total nonreciprocity [17–23], i.e., it propagates only in one direction determined by the chirality of the FA dispersion. Furthermore, a smooth surface of a topological material is known to host massive states called *Volkov-Pankratov* (VP) states [24–29], along with the protected topological chiral states. These gapped bands can be visualized as pseudo-Landau levels of the system where the smoothness of the

interface is modeled as a pseudomagnetic field [30]. Though not protected topologically, their presence may heavily modify the transport [31] and magneto-optical properties [32,33] of surfaces of topological materials.

Here we show within a simple single-boundary model and the *random-phase approximations* (RPA) how the FA and the VP states conspire to give rise to new plasmon modes on a smooth surface of a WSM. We confirm that the FA plasmon is chiral and exhibits strong anisotropy and a singularity at zero momentum [17,18,20–23] because the 2D dispersion of the FA band evolves into an effectively 1D one: The energy disperses linearly perpendicular to the  $z$  direction connecting two Weyl nodes and remains almost constant along  $z$ . A spectacular consequence of this anisotropy is the finite gap which the FA plasmon acquires at  $q_z = 0$  and that vanishes for longitudinal wave-vectors  $q_z \neq 0$ . Moreover, a VP intraband plasmon appears when the chemical potential is above the minimum of the first VP band. Somewhat surprisingly, this plasmon is also nonreciprocal in spite of the  $k_y \leftrightarrow -k_y$  symmetric dispersion of the VP bands. As we show below, this is due to coupling to the chiral FA state. We also find a gapped plasmon mode that stems from excitations between two VP bands of the same band index and that we call *VP interband plasmon*.

### II. SMOOTH WSM SURFACE

We consider a smooth interface in the  $x$  direction between a time-reversal breaking WSM and a trivial insulator modeled by the Hamiltonian valid between  $0 \leq x \leq \ell$  [33–35],

$$H = v(k_x \sigma_x + k_y \sigma_y) + \left( \frac{k_z^2}{2m} - \Delta + 2 \frac{\Delta}{\ell} x \right) \sigma_z, \quad (1)$$

where  $v$ ,  $m$ , and  $\Delta$  are the Fermi velocity, effective mass, and the magnitude of the inverted gap, respectively. These material-related parameters are positive and henceforth we use  $\hbar = 1$  for notational simplicity. Without the  $x$ -dependent term, this is the simplest model for a time-reversal breaking

two-node WSM with Weyl nodes at  $\mathbf{k} = \eta\sqrt{2m\Delta}\hat{z}$  with opposite chirality  $\eta = \pm 1$ . The spatially varying gap parameter describes explicitly how the inverted band gap at the center of Brillouin zone is closed and reopened across the interface of width  $\ell$  from a WSM ( $x < 0$ ) to a trivial insulator ( $x > \ell$ ). The smoothness of the surface can be viewed as an effective chiral pseudomagnetic field  $\mathbf{B}_P = -\eta 2\Delta/ev\ell\hat{y}$  that couples to the two Weyl nodes of opposite chirality with respective signs. Hamiltonian (1) can be diagonalized by introducing creation and annihilation operators constructed from linear combinations of the  $k_x$ - and the  $x$ -dependent terms. Thus, the effective surface bands are reminiscent of Landau levels following the dispersion [35,36]

$$E_n^\lambda(k_y) = \lambda v \sqrt{k_y^2 + \frac{2n}{\ell_S^2}} = \lambda \sqrt{v^2 k_y^2 + n e_0^2}, \quad (2)$$

for  $n \geq 1$ , where  $\lambda = \pm$  is the band index, and the smoothness of the surface has been encoded in an effective magnetic length  $\ell_S = 1/\sqrt{eB_P}$ . The VP band gap  $e_0 = \sqrt{2}v/\ell_S$ , which is the separation between the  $n = 0$  and the  $n = 1$  bands at  $\mathbf{k} = 0$ , sets the characteristic energy scale of this surface model. The FA is naturally described by the  $n = 0$  band with

$$E_0(k_y) = vk_y, \quad (3)$$

and breaks the symmetry  $k_y \rightarrow -k_y$ , its counterpart with opposite sign of the dispersion being localized at the other surface of the WSM that we do not consider here. The FA state is independent of the surface details such as its smoothness, i.e., the band dispersion does not depend on  $\ell$ , indicating its topological nature. However, the  $n \geq 1$  VP bands depend strongly on the surface modeling. In the sharp-surface limit ( $\ell \rightarrow 0$ ), the VP bands rise up in energy and eventually merge with the bulk states when  $v\sqrt{2n}/\ell_S \sim \Delta$ , while only the FA state survives.

From Eq. (2), we can see that the VP bands are completely flat in the  $k_z$  direction until they hybridize with the bulk Weyl cones, as shown in the inset of Fig. 1. In spite of being embedded in a 2D ( $k_y, k_z$ ) manifold, the VP bands are effectively 1D and thus exhibit van Hove singularities in the density of states at the band extrema. The underlying 2D nature and the  $k_z$  dependence is encoded in the location of the surface states: Along the interface, they have a Gaussian profile of a characteristic width  $\ell_S$  centered at  $\langle x \rangle = B_P(\Delta - k_z^2/2m)$ . This, as shown below, results in nondiagonal overlap matrix elements for excitations in the  $k_z$  direction.

### III. QUASI-2D RPA

In order to analyze the behavior of surface electrons, consider the noninteracting dynamical polarization

$$\chi_{i,j}^{(0)}(\mathbf{q}, \omega) = \frac{1}{V} \sum_{\mathbf{k}} \frac{f_D[E_i(\mathbf{k})] - f_D[E_j(\mathbf{k} + \mathbf{q})]}{\omega + E_i(\mathbf{k}) - E_j(\mathbf{k} + \mathbf{q}) + i\delta} \times |F_{i,j}(\mathbf{k}, \mathbf{k} + \mathbf{q})|^2, \quad (4)$$

where  $\delta = 0^+$  and the  $i, j$  indices are shorthand notations for both band labels  $n$  and  $\lambda$ . In general, the overlap matrix  $F_{i,j}$  is not diagonal because of the aforementioned  $k_z$  dependence of the eigenstates so that  $\chi_{i,j}^{(0)}$  is generally a tensor. However,

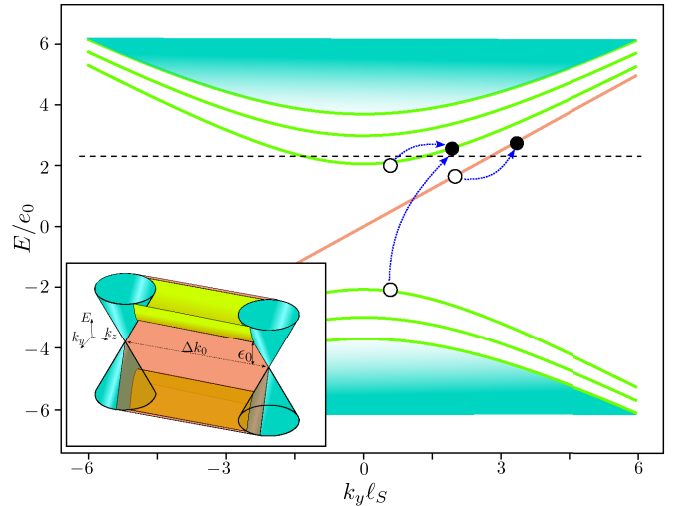


FIG. 1. Various particle-hole excitations involving the surface bands for a fixed transverse momentum. The chiral FA is denoted by the red line, whereas the massive VP bands are shown in green. As discussed in the main text, for  $q_z = 0$ , only  $n \rightarrow \pm n$  excitations are allowed across the Fermi level (dashed line). Inset: Global view on surface bands connecting two Weyl nodes. Along the transverse momentum, the quasi-1D surface bands do not disperse.

for  $q_z = 0$ , the particle-hole excitations are also 1D and  $F_{i,j}$  becomes diagonal, meaning that only excitations from  $n$  to  $\pm n$  are possible. The RPA dielectric function then retrieves its usual form

$$\epsilon^{\text{RPA}}(q_y, \omega) = 1 - V_{2D}(q_y)\chi^{(0)}(q_y, \omega), \quad (5)$$

where  $V_{2D}(q_y) = e^2/2\epsilon_0\epsilon_r|q_y|$ , and  $\chi^{(0)}$  is the noninteracting charge susceptibility, in terms of the environmental dielectric constant  $\epsilon_r$  [36].

When  $q_z \neq 0$ , the overlap matrix element  $F_{i,j}(\mathbf{k}, \mathbf{k} + \mathbf{q})$  is more involved. However, in the long-wavelength limit, the off-diagonal term  $F_{i,j}$  is proportional to  $q_z^{|n_i - n_j|}$  [36] so that the  $n \rightarrow \pm n$  excitations still remain the leading contributions to the charge susceptibility. Nevertheless, due to the complicated form of the off-diagonal terms, we cannot factorize the Coulomb interaction operator [36] even in the long-wavelength limit when several VP bands are present. We therefore consider only the chiral FA and the  $n = \pm 1$  VP bands (*three-band model*), where [36]

$$\chi^{(0)}(\mathbf{q}, \omega) = \sum_{i,j} \chi_{i,j}^{(0)}(\mathbf{q}, \omega), \quad (6)$$

and  $\chi_{i,j}^{(0)}$  are the contributions by the excitation  $(n_i, \lambda_i) \rightarrow (n_j, \lambda_j)$ . Accordingly, we can generalize  $(q_y, \omega)$  in Eq. (5) to  $(\mathbf{q}, \omega)$ .

### IV. PLASMONS

We summarize our results for  $q_z = 0$  in Fig. 2 and for  $q_z \ell_S = 0.2$  in Fig. 3, where we numerically calculate the profile of  $-\text{Im}(\chi^{(0)})$  in the  $(q_y > 0, \omega > 0)$  plane, for different values of the chemical potential  $\mu$  and a given disorder amplitude  $\delta = 0.001e_0$ . Indeed, the imaginary part of  $\chi^{(0)}$  bears important information about possible electronic excitations

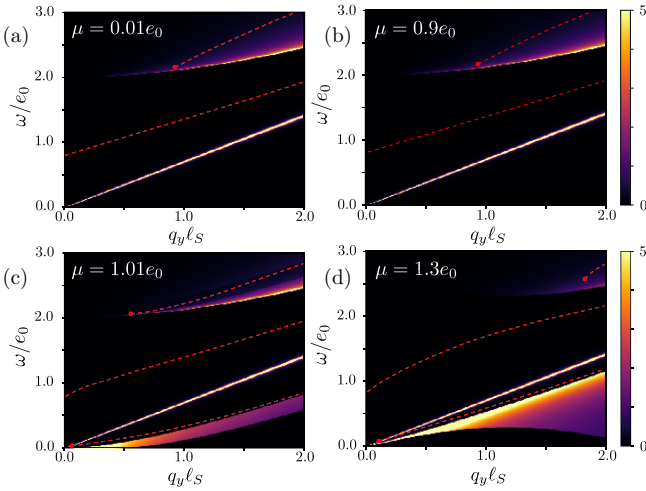


FIG. 2. Profile of the imaginary part of the noninteracting dynamical polarization  $-\text{Im}(\chi^{(0)})$  in the  $(q_y, \omega)$  phase space at  $\mu = 0.01e_0, 0.90e_0, 1.01e_0,$  and  $1.30e_0$  for  $q_z = 0, v = 1 \text{ eV}\cdot\text{\AA}, \ell = 10 \text{ \AA}, \Delta = 1 \text{ eV},$  and  $k_0 = 10 \text{ \AA}^{-1}$ . The zeros of the real part of  $\epsilon^{\text{RPA}}$  (red dashed lines) indicate the plasmon modes.

and therefore damping of the plasmon modes, indicated by the red dashed lines (zeros of the real part of  $\epsilon^{\text{RPA}}$ ). The plasmon modes are only long lived and undamped in the black regions where  $\text{Im}(\chi^{(0)}) = 0$ . Within the above-mentioned three-band model, one obtains three particle-hole continua, with  $-\text{Im}(\chi^{(0)}) \neq 0$ , corresponding to the transitions shown in Fig. 1. The FA particle-hole continuum extends linearly in the  $(q_y > 0, \omega > 0)$  plane. A second particle-hole spectrum is delimited from below by  $\omega > \sqrt{4e_0^2 + v^2q_y^2}$  due to interband excitations involving the VP conduction and valence bands  $n = \pm 1$ , respectively. However, it vanishes at small momenta because the eigenstates associated with the VP conduction and valence bands are orthogonal at  $\mathbf{q} = 0$ .

As we increase  $\mu$  above the VP conduction band [see Figs. 2(c), 2(d), 3(c) and 3(d)], the poles of the FA excitations remain unchanged because of the linear FA dispersion,

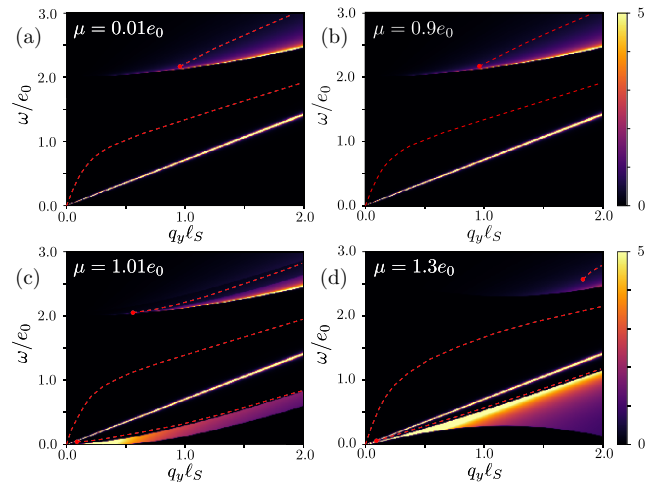


FIG. 3. Same as Fig. 2 except for  $q_z \ell_S = 0.2$ . The zeros of the real part of  $\epsilon^{\text{RPA}}$  (red dashed lines) indicate the plasmon modes

whereas that of the interband particle-hole continua gets heavily modified due to Pauli blocking at the conduction band minima. At low frequencies, intraband excitations of the  $n = +1$  VP band induce a third particle-hole continuum. With  $\mu > e_0$  just above the conduction band minimum, the VP band is approximately parabolic, and its quasi-1D character is apparent in the form of the particle-hole intraband spectrum with its typical exclusion dome for  $q\ell_S < 2k_F$  with  $k_F$  defined as  $\mu = \sqrt{v^2k_F^2 + e_0^2}$ .

In the  $q_z = 0$  limit, two plasmon modes are present for  $\mu < e_0$  as we can see in Figs. 2(a) and 2(b). The first one is the linearly dispersing FA plasmon with a gap at  $q_y = 0$ , in agreement with theoretical approaches using classical electrodynamics [17], hydrodynamic description [22], or quantum-mechanical calculations [18,20,21,23]. From the zeros of the real part of the equation  $\epsilon^{\text{RPA}}(q_y, \omega) = 0$ , we find the FA-plasmon dispersion

$$\omega \approx \text{sgn}(q_y) \frac{k_0 e^2}{4\pi^2 \epsilon_0 \epsilon_r} + \left( 1 + \frac{2k_F}{\sqrt{k_F^2 + \frac{2}{\ell_S^2}}} \delta_{n_F,1} \right) v q_y, \quad (7)$$

where  $2k_0 = 2\sqrt{2m\Delta}$  is the separation between two Weyl nodes in the bulk,  $\epsilon_0$  is the vacuum, and  $\epsilon_r$  is the relative permittivity, while  $n_F$  is the integer part of the ratio between  $\mu$  and  $e_0$ . Let us first focus on the case where  $n_F = 0$ . For positive  $\omega$ , the FA plasmon is allowed to propagate only in the direction of positive  $q_y$ , due to the chirality of the FA. For the usual 2D electron gas or graphene, recall that their plasmon dispersion is square root due to the Coulomb potential being 2D. In spite of the the quasi-1D nature of the FA, the Coulomb potential remains 2D here, and one might naively expect a square-root plasmon dispersion. Surprisingly, this is not the case, and one finds a *linear gapped* plasmon mode thanks to its chiral nature. In spite of its simplicity, Eq. (7) accurately describes the mode found numerically in Figs. 2(a) and 2(b), even when the  $n = \pm 1$  VP states are retained in the calculation. We emphasize that the experimentally measurable FA plasmon gap,

$$\gamma = \frac{k_0 e^2}{4\pi^2 \epsilon_0 \epsilon_r}, \quad (8)$$

yields direct information about the separation  $2k_0$  of the bulk Weyl nodes.

VP intraband excitations significantly modify the dispersion of the FA plasmon when  $n_F = 1$ . The dispersion of FA plasmon at large  $q_y$  remains almost linear with the same velocity  $v$ . At small  $q_y$ , although the gap sticks to the same value  $\gamma$  in Eq. (8), the FA plasmon acquires an enhanced velocity that can be further boosted by increasing the chemical potential as shown in Figs. 2(c) and 2(d). However, the change of velocity for finite  $q_y$ , as seen in Fig. 2, is not captured by Eq. (7).

Since the bands are effectively 1D, the particle-hole continua are independent of  $q_z$  if the coupling between FA and VP bands is omitted, as shown in Fig. 3. It is indeed legitimate to neglect this coupling in the long-wavelength limit where it scales as  $\sim (q_z \ell_S)^2$ . However, the plasmon dispersion gets strongly modified for  $q_y < q_z$  due to the  $q_z$  dependence of the Coulomb interaction. Neglecting a small hybridization between the VP bands and the FA [36], the FA-plasmon gap

at small momenta becomes

$$\gamma' \approx \gamma \frac{q_y}{\sqrt{q_y^2 + q_z^2}}. \quad (9)$$

When  $q_z = 0$ , Eqs. (9) and (8) coincide, and the FA plasmon is gapped as shown earlier. However when  $q_z \neq 0$ , the gap vanishes at  $q_y = 0$  as a consequence of the strong anisotropy of the FA state, which is only quasi-1D but embedded in a 2D manifold. When  $q_y \gg q_z$ , the FA plasmon disperses again linearly with slope  $v$ . This is further validated by our numerical calculations (see Fig. 3): The FA plasmon gap vanishes when  $\mathbf{q} = q_z \hat{z}$ . This singular behavior of the gap at  $\mathbf{q} = 0$  is also reported in Refs. [17,18,20–23].

The second plasmon mode in Figs. 2(a) and 2(b) is the VP interband plasmon, which stems mostly from the  $n = \pm 1$  interband excitations. It is also gapped and starts at a finite momentum for the same orthogonality reason that makes the spectral weight of the particle-hole continuum vanishingly small at  $q_y \sim 0$ , which makes sustained plasmonic oscillations impossible. The interband VP plasmon mode lies in the VP interband particle-hole region and is thus Landau-damped. However, since the amplitude of  $-\text{Im}(\chi^{(0)})$  drops at high energy, this plasmon may be visible as an additional bump in Electron Energy Loss Spectroscopy (EELS), as we show later.

It is interesting to point out that the spectrum in Fig. 2(b), where  $\mu = 0.9e_0$ , is exactly the same as that of Fig. 2(a), where the chemical potential is very close to the charge neutrality point. Indeed the interband excitations between the VP bands are unchanged as long as the chemical potential remains between the two VP bands.

A third plasmon mode emerges when  $\mu > e_0$  [see Figs. 2(c), 2(d) 3(c), and 3(d)]. Interestingly, this mode exists in a region delimited by the particle-hole continua of the FA and the VP conduction bands. It starts at small but finite momentum and its energy disperses along with the upper boundary of the intraband continuum and eventually gets merged in it at larger momentum. One may naively think that this VP intraband plasmon originates only from intraband transitions and has a square-root dispersion at small momenta [36]. However, our numerical calculations invalidate this picture, and one needs to take into account the other particle-hole continua, namely, the linear one associated with the FA, which prohibits such a square-root dependence of an undamped plasmon. Moreover, remote VP interband excitations do not only modify  $\epsilon_r$  in the low-energy modes because of the diverging density of states when the chemical potential crosses a VP conduction band. This significantly modifies the dynamical screening and, as shown in Fig. 2, the VP intraband plasmon acquires positive energy only at nonzero finite momentum and disperses linearly with a velocity smaller than  $v$ . Increasing  $\mu$  from 1.01 to 1.3 $e_0$ , the exclusion dome at low frequencies becomes wider. The available phase space for the VP intraband plasmon between the FA and the VP intraband continua reduces even further, making this plasmon less visible at larger values of  $\mu$ .

## V. NONRECIPROCALITY

To show what one can see in experiments, we plot in Fig. 4 electron loss function  $-\Im[1/\epsilon^{\text{RPA}}]$ , measurable by EELS, in

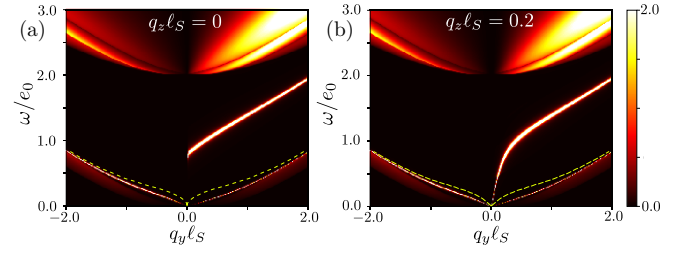


FIG. 4. Electron loss function at  $\mu = 1.01e_0$  for  $q_y l_S \in [-2.0, 2.0]$ : Left for  $q_z = 0$  and right for  $q_z l_S = 0.2$ . Yellow dashed lines show the symmetric VP intraband plasmon in the absence of the FA state. Three plasmon modes are all nonreciprocal and visible.

( $q_y, \omega > 0$ ) plane with intensity indicated by the colorbar. One of the intriguing properties of the FA plasmon is its nonreciprocity, reflecting the chiral nature of the FA state. Therefore, we should also study  $-\Im[1/\epsilon^{\text{RPA}}]$  for ( $q_y < 0, \omega > 0$ ). The result for  $\omega < 0$  can be found easily by reversing simultaneously the sign of  $\omega$  and  $\mathbf{q}$  in known results. As shown in Fig. 4 where  $\mu = 1.01e_0$ , the FA plasmon is completely absent when  $q_y < 0$  as well as the corresponding particle-hole continuum. Being nonreciprocal, FA plasmon only propagates in one direction with fixed velocity, highly desirable for applications. Strikingly, also the VP intraband plasmon is nonreciprocal even if it involves the  $k_y \leftrightarrow -k_y$  symmetric  $n = \pm$  VP bands [see Eq. (2)]: It has a different dispersion for  $q_y < 0$ , which can be calculated analytically there

$$\omega \approx \text{sgn}(-q_y)v \left( |q_y| + \frac{2k_F}{\sqrt{k_F^2 + \frac{2n}{\ell_3^2}}} \sqrt{q_y^2 + q_z^2} \right). \quad (10)$$

Contrary to  $q_y > 0$ , it starts from the origin of ( $q_y, \omega$ ) and disperses with a velocity larger than  $v$  which can be enhanced further by increasing  $\mu$ . This nonreciprocity is a consequence of the hybridization with the FA mode and particle-hole continuum, which is in close vicinity of the intraband VP plasmon for  $q_y > 0$  but further well separated in energy for  $q_y < 0$  [36]. The chirality of the FA modes thus induces a nonreciprocity in the other excitations due to their mutual coupling. This can also be seen in the VP interband plasmon, where the starting point moves to higher energies and larger momenta. As anticipated above, the VP interband plasmon is submerged amid particle-hole continuum but nevertheless visible on EELS.

## VI. DISCUSSION

We have investigated the effect of surface smoothness on the charge oscillation spectrum of a WSM surface. Within RPA calculations, we observe the emergence of two collective modes stabilized by the inter- and intra-VP band excitations, in addition to the FA plasmon. The plasmons exhibit anisotropy and nonreciprocity inherited from the underlying surface model. Our findings could be verified experimentally, e.g., in EELS, which in addition to a proof of these plasmons could probe the chirality of the FA. Furthermore, the plasmon gap in Eq. (8) gives us a direct experimental measure of the separation between the Weyl nodes. Notice that we do not aim to present a complete theory of surface plasmons in WSM, but

we have concentrated here on the role of the surface smoothness and the resulting VP bands. While the qualitative features of the different plasmons are robust to other effects, e.g., variations of the surface potential beyond the linear approximation, further studies are required to investigate these effects. As an example, one may invoke the curvature of the FA, which is expected to enhance its density of states [35] and thus the gap (8). Finally, one may invoke anisotropies of the bulk Weyl cones, e.g., and anisotropic Fermi velocity or tilts. Notice that they only affect the FA if these anisotropies are different in the two cones, the FA being tangential to the cones. However, the third (intra-VP) plasmon loses its  $q_y \leftrightarrow -q_y$  symmetry, as

it has been shown in 2D tilted and anisotropic Dirac materials [37–40].

### ACKNOWLEDGMENTS

We acknowledge financial support from Agence Nationale de la Recherche (ANR project “Dirac3D”) under Grant No. ANR-17-CE30-0023. D.K.M. acknowledges partial financial support from NSF Grant No. DMR-1914451 and the Research Corporation for Science Advancement through a Cottrell SEED award.

- 
- [1] N. P. Armitage, E. J. Mele, and A. Vishwanath, *Rev. Mod. Phys.* **90**, 015001 (2018).
- [2] S. Das Sarma and E. H. Hwang, *Phys. Rev. Lett.* **102**, 206412 (2009).
- [3] M. Lv and S.-C. Zhang, *Int. J. Mod. Phys. B* **27**, 1350177 (2013).
- [4] I. Panfilov, A. A. Burkov, and D. A. Pesin, *Phys. Rev. B* **89**, 245103 (2014).
- [5] J. Hofmann and S. Das Sarma, *Phys. Rev. B* **91**, 241108(R) (2015).
- [6] D. Giri, D. K. Mukherjee, S. Verma, H. A. Fertig, and A. Kundu, [arXiv:2011.06862](https://arxiv.org/abs/2011.06862).
- [7] E. H. Hwang and S. Das Sarma, *Phys. Rev. B* **75**, 205418 (2007).
- [8] B. Wunsch, T. Stauber, F. Sols, and F. Guinea, *New J. Phys.* **8**, 318 (2006).
- [9] D. T. Son and B. Z. Spivak, *Phys. Rev. B* **88**, 104412 (2013).
- [10] J. Zhou, H.-R. Chang, and D. Xiao, *Phys. Rev. B* **91**, 035114 (2015).
- [11] R. H. Ritchie, *Phys. Rev.* **106**, 874 (1957).
- [12] J. Hofmann and S. Das Sarma, *Phys. Rev. B* **93**, 241402(R) (2016).
- [13] T. Tamaya, T. Kato, K. Tsuchikawa, S. Konabe, and S. Kawabata, *J. Phys.: Condens. Matter* **31**, 305001 (2019).
- [14] A. A. Zyuzin and A. A. Burkov, *Phys. Rev. B* **86**, 115133 (2012).
- [15] O. V. Kotov and Y. E. Lozovik, *Phys. Rev. B* **98**, 195446 (2018).
- [16] F. M. D. Pellegrino, M. I. Katsnelson, and M. Polini, *Phys. Rev. B* **92**, 201407(R) (2015).
- [17] J. C. W. Song and M. S. Rudner, *Phys. Rev. B* **96**, 205443 (2017).
- [18] G. M. Andolina, F. M. D. Pellegrino, F. H. L. Koppens, and M. Polini, *Phys. Rev. B* **97**, 125431 (2018).
- [19] Ž. B. Lošić, *J. Phys.: Condens. Matter* **30**, 365003 (2018).
- [20] F. Adinehvand, Z. Faraei, T. Farajollahpour, and S. A. Jafari, *Phys. Rev. B* **100**, 195408 (2019).
- [21] Q. Chen, A. R. Kutayiah, I. Oladyskin, M. Tokman, and A. Belyanin, *Phys. Rev. B* **99**, 075137 (2019).
- [22] E. V. Gorbar, V. A. Miransky, I. A. Shovkovy, and P. O. Sukhachov, *Phys. Rev. B* **99**, 155120 (2019).
- [23] S. Ghosh and C. Timm, *Phys. Rev. B* **101**, 165402 (2020).
- [24] B. A. Volkov and O. A. Pankratov, *JETP Lett.* **42**, 178 (1985).
- [25] O. Pankratov, S. Pakhomov, and B. Volkov, *Solid State Commun.* **61**, 93 (1987).
- [26] S. Tchoumakov, V. Jouffrey, A. Inhofer, E. Bocquillon, B. Plaçais, D. Carpentier, and M. O. Goerbig, *Phys. Rev. B* **96**, 201302(R) (2017).
- [27] A. Inhofer, S. Tchoumakov, B. A. Assaf, G. Fève, J. M. Berroir, V. Jouffrey, D. Carpentier, M. O. Goerbig, B. Plaçais, K. Bendias, D. M. Mahler, E. Bocquillon, R. Schlereth, C. Brüne, H. Buhmann, and L. W. Molenkamp, *Phys. Rev. B* **96**, 195104 (2017).
- [28] D. J. Alspaugh, D. E. Sheehy, M. O. Goerbig, and P. Simon, *Phys. Rev. Res.* **2**, 023146 (2020).
- [29] T. L. van den Berg, A. De Martino, M. R. Calvo, and D. Bercioux, *Phys. Rev. Res.* **2**, 023373 (2020).
- [30] X. Lu and M. O. Goerbig, *Phys. Rev. B* **102**, 155311 (2020).
- [31] T. L. van den Berg, M. R. Calvo, and D. Bercioux, *Phys. Rev. Research* **2**, 013171 (2020).
- [32] X. Lu and M. O. Goerbig, *Europhys. Lett.* **126**, 67004 (2019).
- [33] D. K. Mukherjee, D. Carpentier, and M. O. Goerbig, *Phys. Rev. B* **100**, 195412 (2019).
- [34] R. Okugawa and S. Murakami, *Phys. Rev. B* **89**, 235315 (2014).
- [35] S. Tchoumakov, M. Civelli, and M. O. Goerbig, *Phys. Rev. B* **95**, 125306 (2017).
- [36] See supplemental material at <http://link.aps.org/supplemental/10.1103/PhysRevB.104.155103> for more details.
- [37] T. Nishine, A. Kobayashi, and Y. Suzumura, *J. Phys. Soc. Jpn.* **79**, 114715 (2010).
- [38] J. Sári, C. Tóke, and M. O. Goerbig, *Phys. Rev. B* **90**, 155446 (2014).
- [39] Z. Jalali-Mola and S. A. Jafari, *Phys. Rev. B* **102**, 245148 (2020).
- [40] R. Hayn, T. Wei, V. M. Silkin, and J. van den Brink, *Phys. Rev. Mater.* **5**, 024201 (2021).